PAN

Opto-Electronics Review

journal homepage: https://journals.pan.pl/opelre

Growth and characterisation of LWIR T2SL on (100)-, (211)- and (311)-oriented GaSb substrates

Dmitri Lubyshev[1*], Joel M. Fastenau[1], Michael Kattner[1], Philip Frey[1], Scott A. Nelson[1], Ryan Flick[1], Ying Wu[1], Amy W. K. Liu[1], Dennis E. Szymanski[1], Becky Martinez[2], Mark J. Furlong[2], Richard Dennis[3], Jason Bundas[3], Mani Sundaram[3]

[1]IQE, Inc., 119 Technology Dr., Bethlehem, PA 18015, USA
[2]IQE, Pascal Close, St. Mellons, Cardiff, CF3 0LW, UK
[3]QmagiQ, LCC, 22 Cotton Rd., Unit H, Suite 180, Nashua, NH 03063, USA

Article info

Article history:
Received 28 Oct. 2022
Received in revised form 10 Dec. 2022
Accepted 19 Dec. 2022
Available online 24 Feb. 2023

Keywords:
Focal plane arrays; InAs/InAsSb photodetectors; long wavelength infrared type-II superlattice; metamorphic buffers; superlattice period reduction.

Abstract

Ga-free InAs/InAsSb type-II superlattice structures grown on GaSb substrates have demonstrated high performance for mid-wave infrared applications. However, realisation of long wavelength infrared photodetectors based on this material system still presents challenges, especially in terms of reduced quantum efficiency. This reduction is due, in part, to the increased type-II superlattice period required to attain longer wavelengths, as thicker periods decrease the wave-function overlap for the spatially separated quantum wells. One way to improve long wavelength infrared performance is to modify the type-II superlattice designs with a shorter superlattice period for a given wavelength, thereby increasing the wave-function overlap and the resulting optical absorption. Long wavelength infrared epitaxial structures with reduced periods have been realised by shifting the lattice constant of the type-II superlattice from GaSb to AlSb. Alternatively, epitaxial growth on substrates with orientations different than the traditional (100) surface presents another way for superlattice period reduction. In this work, the authors evaluate the performance of long wavelength infrared type-II superlattice detectors grown by molecular beam epitaxy using two different approaches to reduce the superlattice period: first, a metamorphic buffer to target the AlSb lattice parameter, and second, structures lattices matched to GaSb using substrates with different orientations. The use of the metamorphic buffer enabled a ~30% reduction in the superlattice period compared to reference baseline structures, maintaining a high quantum efficiency, but with the elevated dark current related to defects generated in the metamorphic buffer. Red-shift in a cut-off wavelength obtained from growths on high-index substrates offers a potential path to improve the infrared photodetector characteristics. Focal plane arrays were fabricated on (100), (311)A- and (211)B-oriented structures to compare the performance of each approach.

1. Introduction

InAs/InAsSb (also referred to as Ga-free) type-II superlattice (T2SL) mid-wave infrared (MWIR) barrier photodetectors (PD) have continued to mature, emerging as a disruptive technology to traditional InSb and mercury-cadmium-telluride (MCT) infrared (IR) photodetectors [1–4]. While development of Ga-free long wavelength infrared (LWIR) PDs is ongoing, this material approach for the wavelength range of 8–12 μm remains state-of-the-art. There are important limiting factors that arise for improvement of the Ga-free T2SL LWIR PD figures of merit. Thicker Ga-free superlattice (SL) periods required for LWIR lead to a reduction of wave-function overlapping [5] meaning reduced absorption coefficient [6] and quantum efficiency (QE). Traditionally, improvements in

*Corresponding author at: dloubychev@iqep.com

https://doi.org/10.24425/opelre.2023.144568
1896-3757/ Association of Polish Electrical Engineers (SEP) and Polish Academic of Sciences (PAS). Published by PAS

LWIR InAs/InAsSb T2SLs are based on optimization of device architecture, specifically absorber layer design, as well as improvement of material quality [7, 8].

A parallel technology to the InAs/InAsSb T2SL is the GaSb/InAs T2SL. The GaSb/InAs T2SL design approach results in thinner superlattice periods for the same wavelength compared to the Ga-free superlattice. This is an inherent advantage for the GaSb/InAs T2SL as the thinner periods improve wave-function overlap, providing potential increase of absorption coefficient and QE. However, as analysed in Ref. 9, the advantage of enhanced wave-function overlap is negated by the smaller minority carrier lifetimes in InAs/GaSb T2SLs as compared to the InAsSb/InAs T2SLs. Minority carrier lifetimes for InAs/GaSb T2SLs are on the order of 100 ns at 110 K [10]. Whereas InAs/InAsSb T2SLs have a minority carrier lifetime of approximately 10 µs [11] at 80 K. Additionally, the InAs/GaSb T2SL growth procedure and strain-balance control is significantly more complicated.

In this work, the authors focused on the possibility to reduce T2SL period in the InAs/InAsSb material system to improve wave-function overlapping and increase absorption coefficient. Two different approaches were used to accomplish this task: (1) growth of a metamorphic buffer on a (100) GaSb substrate to obtain the AlSb lattice parameter as offered in Ref. 12, (2) utilization of (211)- and (311)-oriented GaSb substrates to promote a red-shift in the wavelength compared to growing the exact same SL period on a (100) substrate. This red-shift may be attributed to a piezoelectric effect [1, 2] for the InAs/InAsSb T2SLs on the higher orientation substrates.

2. Experimental procedures

The LWIR photodetector structures examined in this work employed the generic nBn contact-barrier-absorber architecture and were grown by a solid-source molecular beam epitaxy (MBE). This architecture includes the following layers: buffer, thick Ga-free T2SL absorber, AlGaAsSb-based barrier, and top T2SL contact. The undoped InAs/InAsSb T2SL absorber period ranged from 60 to 120 Å, depending on the experimental growth approach, with a total absorber thickness of 3–4 µm [2].

Baseline nBn structures were grown lattice-matched on (100) GaSb substrates using a simple GaSb buffer. For growth approach (1), a metamorphic buffer (M-buffer) was inserted to modify the lattice constant from GaSb (6.09 Å) out to that of AlSb (6.14 Å). The M-buffer included a GaSb/AlSb dislocation filtering superlattice and a thick AlSb layer. This metamorphic nBn (M-nBn) structure included a modified T2SL design to match a T2SL to the AlSb lattice parameter. For the authors' growth approach (2), the same baseline nBn designs were grown directly on the higher-orientation substrates with a simple GaSb buffer, often in the exact same epitaxial growth run in order to provide direct material performance comparisons.

All epitaxial growths in this work were performed on an Oxford VG V-100 production MBE tool using a process developed and optimized at IQE for Sb-based IR PD structures grown on (100) GaSb substrates. To ensure identical V/III ratios and substrate temperatures, the 3-inch diameter GaSb substrates with different orientations were located in equivalent planetary positions on a multi-wafer substrate holder, ensuring that the exact same deposition takes place on each wafer. Details of the MBE reactor configuration, growth conditions, and *in situ* monitoring tools have been previously described [2, 13, 14].

A variety of characterisation techniques were applied to evaluate surface morphology, structural properties, and optical quality of the epitaxial material. Surface morphology was evaluated using a Nomarski contrast optical microscope and a Veeco D500 atomic force microscope (AFM). Epitaxial layer structure quality, alloy composition, and SL period were measured using high-resolution x-ray diffraction (HRXRD), utilizing the (004) reflection for (100) substrates; the (113) reflection for (311) substrates; and the (224) reflection for (211) substrates. Simulation software was used to determine alloy compositions and superlattice periods. X-ray diffraction (XRD) reciprocal mapping was used to evaluate plastic relaxation for the metamorphic structures.

Photoluminescence (PL) data were acquired at 77 K using a Nicolet FTIR-8700 spectrometer in a double modulation configuration with an EO Systems MCT detector. Evaluation of QE, cut-off wavelength, and dark current density (J_d) were conducted by fabrication and testing of large area photodetectors. Standard optical lithography and wet chemical etching processes were utilized, creating variable size mesa diodes. The fabrication process does not include anti-reflection coating or passivation. Test chips were wire-bonded and packaged in chip carriers for diode measurements, which were performed at 82 K via front-side flood illumination. Current density *vs*. voltage (*J-V*) data were collected in an SE IR optical test dewar. QE as a function of bias and wavelength was measured using a precision source-meter to apply a bias, a preamplifier, an optical chopper, and a lock-in amplifier. This setup measures the photocurrent generated by the cavity blackbody. Finally, selected epitaxial structures on (100), (311)A, and (211)B substrates were fabricated for a full focal plane array (FPA) testing and evaluation.

3. Results and discussion

3.1. T2SL structures grown using metamorphic buffer

The LWIR InAs/InAsSb T2SL absorber design provides great flexibility to tune the absorption bandgap and the strain-balanced lattice constant by independently adjusting the individual T2SL layer thicknesses and the Sb-composition. Growing the T2SL lattice-matched to the GaSb results in a design space constrained to that lattice constant and requires thicker periods and/or higher Sb-composition to achieve longer wavelengths [15, 16]. Using the M-Buffer to move to the T2SL for AlSb lattice constant changes the strain-balance calculations, resulting in a thinner design period to achieve the same wavelength. Using this approach, the authors grew an M-nBn PD structure on a GaSb substrate with the AlSb M-buffer, targeting a wavelength in the 10–11 µm range. The T2SL period required to achieve that wavelength was about 30% smaller compared to the SL with the same Sb-composition grown lattice-matched to GaSb.

M-nBn photodetector structures grown using the AlSb M-buffer displayed smooth, albeit cross-hatched, surface

morphology with low defect density as evidenced by the Nomarski images shown in Fig. 1. AFM root-mean-square (rms) roughness measured 4.2 and 9.3 Å for 5 µm × 5 µm and 20 µm × 20 µm scans, respectively. The minor defect in Fig. 1(d) may be related to a threading dislocation. The 77 K PL spectrum shown in Fig. 2 records a peak wavelength of 10.5 µm which is right on target for the design. Plastic relaxation in this M-nBn was investigated using XRD reciprocal mapping, shown in Fig. 3. A mechanism for plastic relaxation of the structure is the epilayer tilt. The AlSb-based M-buffer was tilted by −386 arcsec from the GaSb substrate, and the T2SL tilt was −590 arcsec from the buffer. The AlSb M-buffer was essentially fully relaxed.

The SL period of 81 Å was measured via an analysis of the (004) HRXRD spectrum (not shown). To achieve the same wavelength with a T2SL lattice-matched to the GaSb would require a period in the 110 to 120 Å range, depending on the Sb-composition. Thus, by using the AlSb M-buffer the authors have reduced the SL absorber period by approximately 30%.

Material quality and photodiode device performance was evaluated by a large-area mesa diode fabrication and testing. Characteristic curves for J_d, QE *vs.* bias, and spectral response of the M-nBn are shown in Fig. 4. The measured cut-off wavelength of 10.5 µm, extracted from the spectral curve, aligns with the 77 K PL wavelength. The M-nBn detectors exhibited a relatively high J_d value of $2 \cdot 10^{-3}$ A/cm^{-2} at a turn-on voltage (V_{on}) of −0.2 V. At higher reverse bias, the current jumps as tunnelling becomes dominant. This tunnelling current is higher than seen in baseline structures grown lattice-matched to GaSb. The most likely mechanism is transport through dislocations and defects originating in the M-buffer which then propagate into the absorber layer. Further optimization of the metamorphic buffer design is needed in order to reduce the defect density and threading dislocations which increase the J_d for these PDs. Despite the increased tunnelling, the M-nBn provides a robust peak QE of 45% at V_{on}, which is very comparable to the baseline structures. This maintaining of a high QE may be partially credited to the increased absorption wave-function overlap provided by the reduced T2SL period in the AlSb metamorphic structure.

3.2. *T2SL structures grown lattice-matched on (100)-, (211)- and (311)-oriented substrates*

Observed wavelength red-shifts and band gap narrowing in InAs/InAsSb T2SL structures grown on (n11)-oriented substrates may arise from multiple mechanisms. These include: layer thickness undulation, lateral InAsSb alloy composition modulation, InAsSb alloy ordering, presence of a piezoelectric field, variation of optical matrix elements with orientation change from (100) toward (111), or a combination thereof [2, 3]. Typically, the presence of layer thickness undulation and lateral alloy composition modulation can be determined by the HRXRD analysis. As none were observed in the material presented here, those mechanisms may be eliminated.

To investigate potential effects of ternary alloy ordering, the authors grew a binary InAs/GaSb T2SL with varying SL periods on (311) GaSb substrates (Fig. 5).

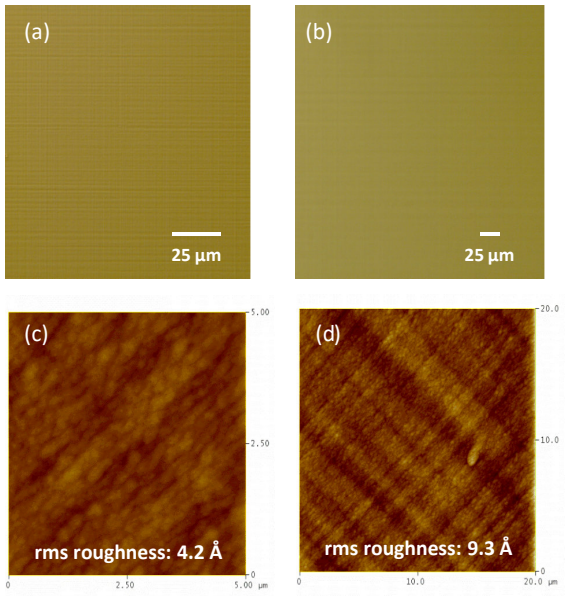

Fig. 1. Nomarski images at ×200 (a) and ×500 (b) magnification; and AFM images for 5×5 µm (c) and 20×20 µm (d) scans for T2SL M-nBn structures grown on (100) GaSb using the AlSb M-buffer.

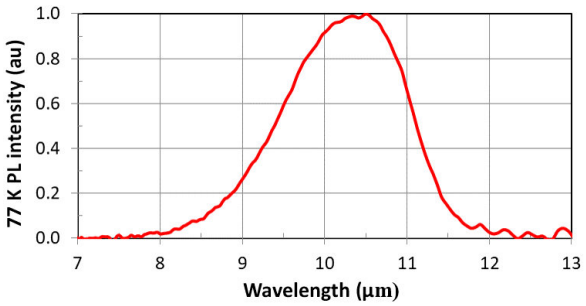

Fig. 2. 77 K PL spectrum for the T2SL M-nBn structure at the AlSb lattice constant.

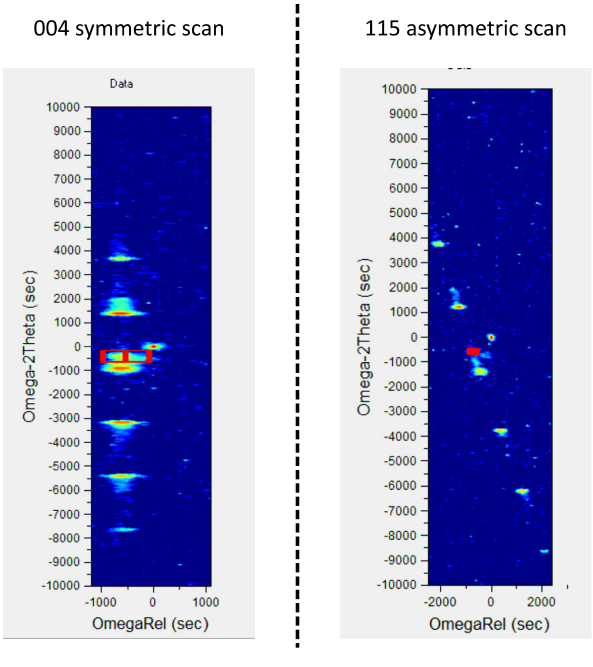

Fig. 3. HRXRD reciprocal maps for T2SL M-nBn grown using the AlSb M-buffer.

Interestingly, the binary SL material grown on (311)A orientation displays no measurable PL signal. However, a binary T2SL material grown on (311)B substrate orientation has a strong PL signal, and measurements showed a red-shift of 1.3–2.1 μm compared to the same binary T2SL material grown on (100) GaSb substrates. Qualitatively, this result coincides with data presented in Ref. 17 for InAs/GaSb T2SL grown on (311)B substrates. This result excludes the possibility of alloy ordering as a mechanism for the red-shift in the higher orientation substrates, and leaves one with internal piezoelectric fields as the most probable mechanism.

3.3. *Structural and optical properties of InAs/InAsSb nBn structures on various orientation substrates*

Photodetector structures on (311)A- and (211)B-oriented substrates were grown side-by-side with reference material on (100) substrates. In all wafers, Nomarski and AFM analysis demonstrated good morphology with no evidence of faceting or surface corrugation, and with a low surface roughness in the range of 1.3 Å to 1.6 Å. Table 1 provides a summary of PL peak wavelength and 82 K large-area photodiode performance parameters grouped as a function of T2SL thickness. For ease of comparison, the J_d and QE data were normalized to the reference material grown on (100) GaSb. PL and diode cut-off wavelength for structures grown on (311)A- and (211)B-oriented substrates showed a red-shift compared to material grown on (100)-oriented substrates. The higher-orientation wavelengths are plotted against the (100) values in Fig. 6, demonstrating that the red-shift wavelength difference increased with a superlattice period. Thus, the higher-orientation substrates do indeed provide a path to designing thinner T2SL periods for a given target wavelength, enabling increased wavefunction overlap and optical absorption.

Table 1.
T2SL 77 K PL, diode cut-off wavelength, and *J*d and QE normalized to (100) values (grouped by absorber period) for nBn PD structures grown on (100), (311)A, and (211)B GaSb substrates.

Structure (target SL period Å)	Substrate orientation	77 K PL-λ (μm)	82 K λ-cut-off (μm)	82 K J_d @ V_{on} (V)	82 K QE @ V_{on} (%)
MW (55 Å)	(100)	5.5	5.5	Ref.	Ref.
	(311)A	5.4	5.4	2×	1.2×
	(211)B	6.3	6.3	10×	1.1×
LWIR-1 (85 Å)	(100)	6.4	6.5	Ref.	Ref.
	(311)A	6.7	6.5	0.75×	0.8×
	(211)B	8.6	9.5	25×	0.6×
LWIR-2 (112 Å)	(100)	7.9	7.8	Ref.	Ref.
	(311)A	8.3	8.2	1×	0.8×
	(211)B	11.6	11.4	160×	0.8×
LWIR-3 (112 Å)	(100)	8.0	8.2	Ref.	Ref.
	(311)A	8.8	8.3	0.2×	0.8×
	(211)B	~13.3	13+	3×	0.7×

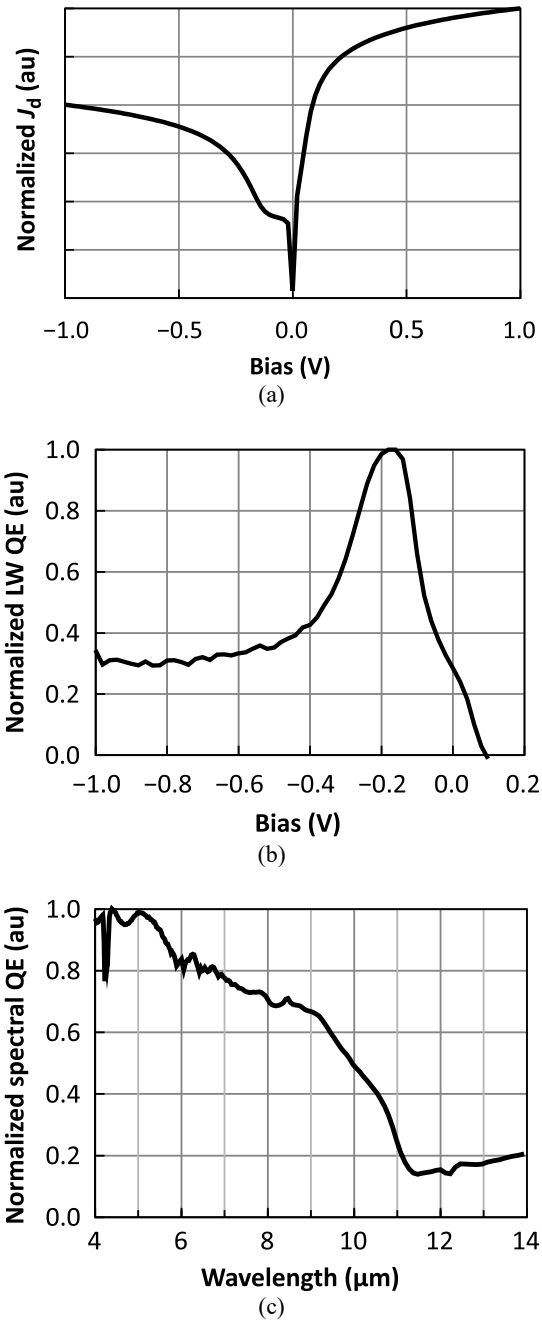

Fig. 4. M-nBn large-area mesa diode test data at 82 K: J_d *vs*. bias (a), QE *vs*. bias (b), and spectral response (c).

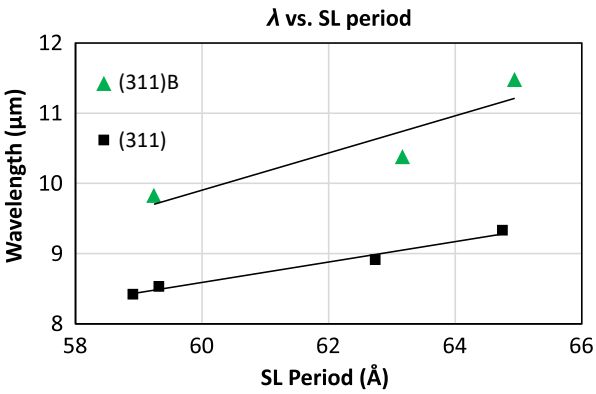

Fig. 5. PL wavelengths *vs*. SL period for InAs/GaSb SL structures grown on (100) and (311)B GaSb substrates.

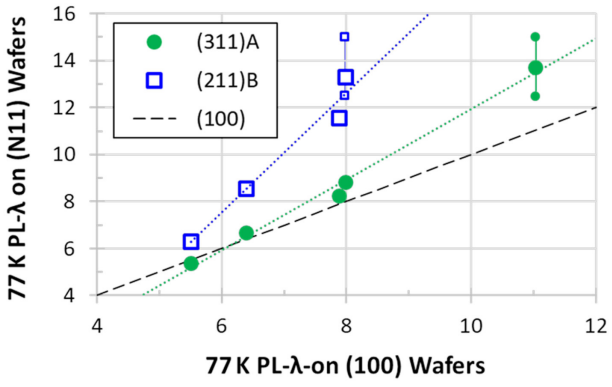

(a)

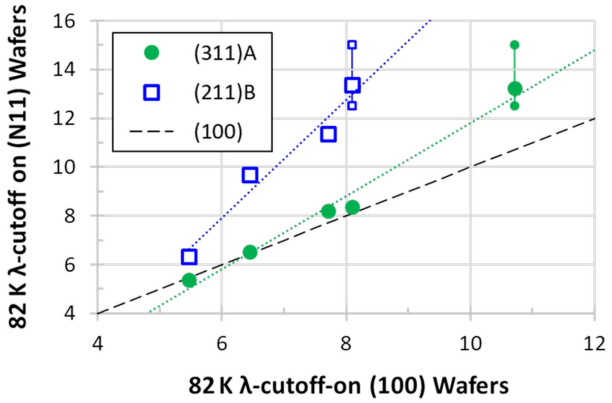

(b)

Fig. 6. InAs/InAsSb nBn substrate orientation-dependent red-shift for 77 K PL (a) and large area photodiode cut-off wavelength (b).

3.4. *FPA array farication on (100), (311)A and (211)B substrates*

Focal plane arrays (FPAs) were fabricated from nBn structures grown on (100), (311)A, and (211)B GaSb substrates, specifically the LWIR-2 epiwafers shown in Table 1. The 320 × 256 pixels, 30 μm pitch process used for FPA fabrication was optimized for (100)-oriented structures. Flat field FPA images presented in Fig. 7 show comparable pixel operability and defect density for all substrate orientations.

Spectral response QE data from the fabricated FPAs is presented in Fig. 8. In agreement with the data from large-area test photodiodes, FPAs fabricated on (311)A- and (211)B-oriented substrates demonstrated red-shift in the

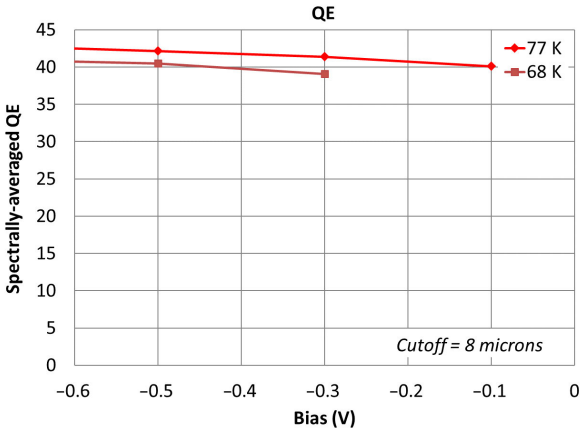

(a)

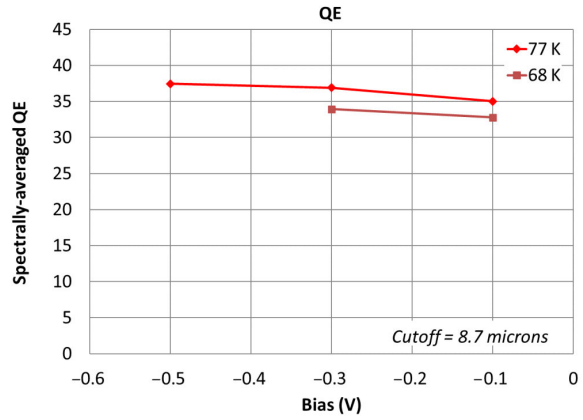

(b)

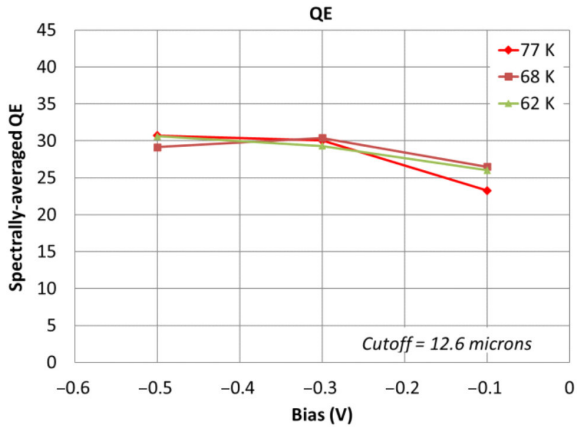

(c)

Fig. 8. Median QE *vs*. bias dependence for FPA on (100) (a), (311)A (b) , and (211)B (c) orientation structures.

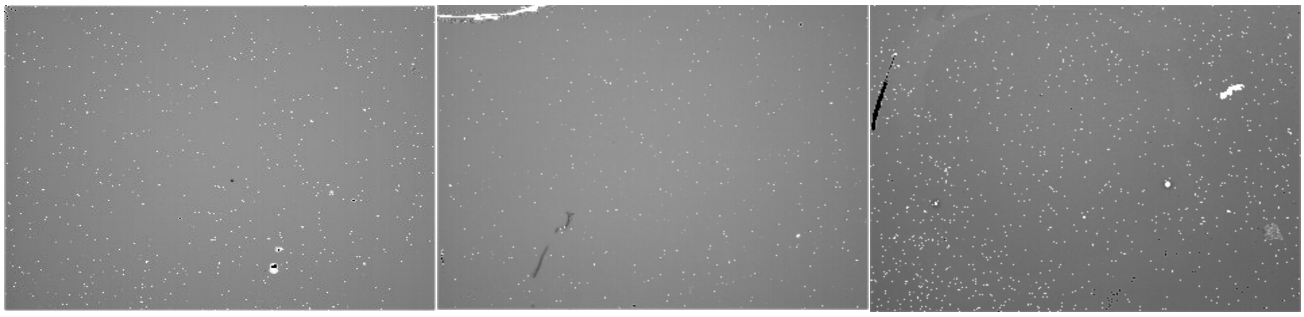

(a) (b) (c)

Fig. 7. Flat-field images for FPAs fabricated on three different GaSb substrate orientations: (100) (a), (311)A (b), and (211)B (c).

cut-off wavelength when compared to a devices grown on (100)-oriented substrates, with the largest red-shift of 4 to 5 μm occurring for devices grown on (211)B-oriented substrates. Such a large change in a cut-off wavelength allows for the design of LWIR T2SL PDs with reduced SL period when compared to PDs grown on (100)-oriented substrates, enhancing wavefunction overlap and, thus, optical absorption and QE.

Median QE *vs*. bias dependence and noise equivalent difference temperature (NEDT) data for fabricated FPAs is presented in Fig. 8 and Fig. 9, respectively. The QE values displayed in Fig. 8 are the average QE values at all wavelengths multiplied by 30 °C Planck function. FPAs on (100)- and (311)A-oriented substrates show a background limited performance (BLIP) floor at 77 K, while the FPA on the (211)B-oriented substrate displayed BLIP floor at 68 K. Average QE values for all FPAs were in the 30–42% range.

The NEDT values for FPAs on (100) and (311)A substrates were 15 mK. In contrast, the NEDT for (211)B FPA varied from 15 to 35 mK as a function of bias and operating temperature. All FPAs demonstrated ~99% pixel operability at low bias.

Temperature dependence of J_d at different biases for (311)A and (211)B FPAs is presented in Fig. 10. While J_d for the (211)B FPA followed the expected trend of reduction of J_d with temperature, the FPA fabricated on (311)A-oriented substrates showed the same character, but only at low bias. At increased bias, J_d did not drop with temperature.

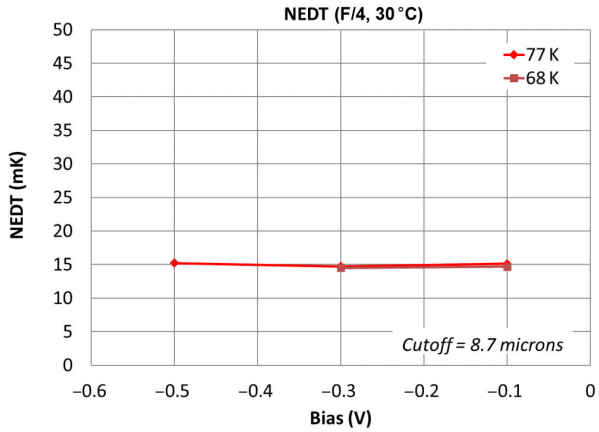

(a)

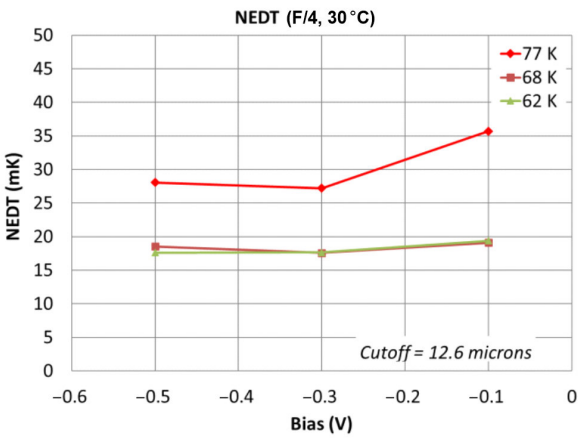

(b)

Fig. 9. NEDT (F/4, 30 °C) data for (311)A- (a) and (211)B- (b) oriented structures.

The J_d image from a (311)A FPA measured at increased bias is shown in Fig. 11. A cross-hatch pattern appears, with an increasing number of leaky pixels at high bias. The nature of such J_d behaviour can be attributed to severe lateral etching of (311)A pixels. However, this hypothesis requires further investigation.

4. Conclusions

In this work, the authors demonstrated T2SL-based LWIR IR photodetectors with reduced period for improved optical absorption. Reduction of the period was

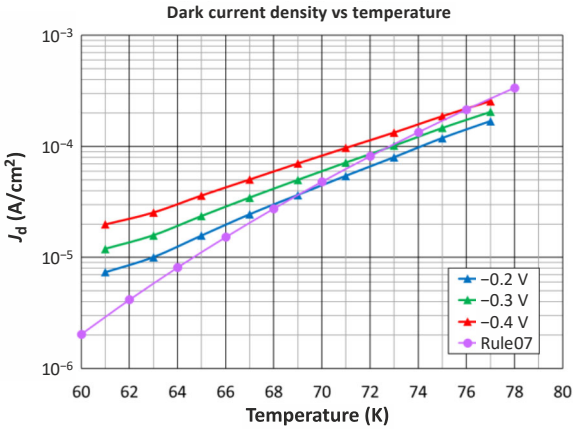

(a)

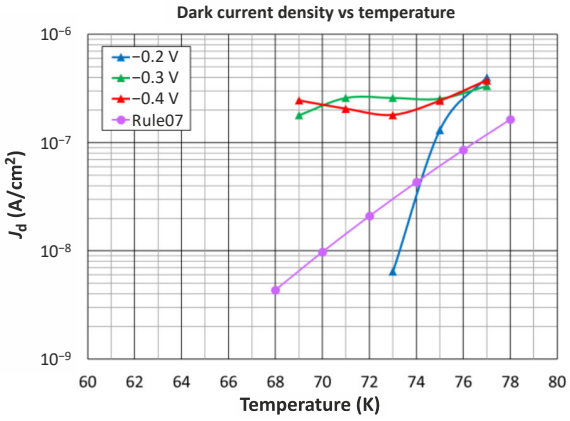

(b)

Fig. 10. Temperature dependence for median dark current J_d for (311)A (a) and (211)B (b). FPA measured at different biases.

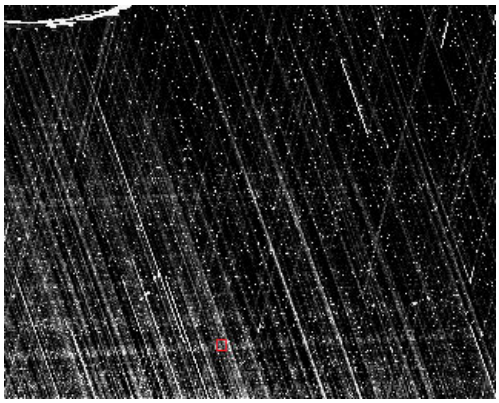

Fig. 11. 77 K J_d image for (311)A FPA at increased bias.

accomplished by shifting lattice constant via growth of a metamorphic buffer, and by growth on high-index GaSb substrates. For nBn structures grown using the AlSb based M-buffer, a ~30% reduction in superlattice period was achieved compared to material lattice-matched to GaSb substrate. Large area test photodiodes demonstrated good QE of 45% at V_{on}, although elevated J_d was observed and attributed to dislocation generation as a result of the mismatched growth. This result is an encouraging proof of the concept for the metamorphic LW T2SL material.

LWIR devices grown on (311)A and (211)B GaSb substrates demonstrate red-shift in the PL and cut-off wavelengths as compared to the same nBn device structure simultaneously grown on a (100) GaSb substrate. As the authors measured only minor variations in SL period and composition, they hypothesize the red-shift may be caused by a built-in piezo-electric field accumulated within the SL on the polar high-index planes. Additional experiments with a binary InAs/GaSb SL allow for the exclusion of the potential CuPt-B alloy ordering effect as the mechanism of band gap reduction in InAsSb/InAs material.

For the first time, high quality LWIR FPAs were fabricated on (311)A- and (211)B-oriented GaSb substrates. These FPAs demonstrated high QE and high pixel operability. FPAs on (311)A show leaky pixels in a cross-hatch pattern when operated at higher bias; this is most likely due to pixel-etch problems in this orientation and can be mitigated by etch optimization. The FPA on the (211)B substrate shows a large, 4 to 5 µm, red-shift in cut-off compared to the FPA on (100). This may be due to different energy bandgap line-up of the superlattice constituent materials.

Both paths investigated here, growth using a metamorphic buffer and growth on high index substrates, offer the opportunity to reduce SL period and increase optical absorption, and, thus, higher QE for LWIR T2SL.

5. Acknowledgements

The authors would like to acknowledge their colleagues at IQE, especially Scott Cramb, Mike Gimbor, Cherrie Lynn Heisey, David Woodward, Elena Crawford, and Joe Adamek, for their contributions to the MBE growth and characterisation of the samples represented in this work.

References

[1] Lubyshev, D. *et al*. Effect of substrate orientation on Sb-based MWIR photodetector characteristics. *Infrared Phys. Technol.* **95**, 27–32 (2018). https://doi.org/10.1016/j.infrared.2018.09.031

[2] Lubyshev, D. *et al*. T2SL mid- and long-wave infrared photodetector structures grown on (211)A, (211)B, and (311)A GaSb substrates. *Proc. SPIE* **11002**, 110020N (2019). https://doi.org/10.1117/12.2521066

[3] Williams, A. & Tidrow, M. III-V infrared focal plane array development in US. *Proc. SPIE* **10624**, 10624OP (2018). https://doi.org/10.1117/12.2311494

[4] Lubyshev, D. *et al*. Manufacturable MBE growth process for Sb-based photodetector materials on large diameter substrates. *Proc. SPIE* **8268**, 82681A (2012). https://doi.org/10.1117/12.909571

[5] Steenbergen, E. H. Strain-balanced InAs-InAsSb Type-II Superlattices on GaSb Substrates for Infrared Photodetector Applications (Arizona State University, 2012).

[6] Manyk, T., Michalczewski, K., Murawski, K., Martyniuk, P. & Rutkowski, J. InAs/InAsSb strain-balanced superlattices for longwave infrared detectors. *Sensors* **19**, 1907 (2019). https://doi.org/10.3390/s19081907

[7] Ting, D. Z. *et. al*. Very Long Wavelength InAs/InAsSb Type-II Superlattice Barrier Infrared Detectors and FPAs. in *15th International Conference on Mid-Infrared Materials and Devices (MIOMD)* 1–10 (2021). https://trs.jpl.nasa.gov/bitstream/handle/2014/55742/CL%2321-3917.pdf?sequence=1

[8] Ting, D. Z. InAs/InAsSb Superlattice Infrared Detectors. in *Quantum Structure Infrared Photodetectors (QSIP) International Conference,Poland* (2022).

[9] Alshahrani, D. O., Kesaria, M., Anyebe, E. A., Srivastava, V. & Huffaker, D. L. Emerging type-II superlattices of InAs/InAsSb and InAs/ GaSb for mid-wavelength infrared photodetectors. *Adv. Photonics Res*. **3**, 2100094 (2022). https://doi.org/10.1002/adpr.202100094

[10] Klein, B. *et al*. Carrier lifetime studies in midwave infrared type-II InAs/GaSb strained layer superlattice. *J. Vac. Sci. Technol. B* **32**, 02C101 (2014). https://doi.org/10.1116/1.4862085

[11] Aytac, Y. *et al*. Effects of layer thickness and alloy composition on carrier lifetimes in mid-wave infrared InAs/InAsSb superlattices. *Appl. Phys. Lett.* **105**, 022107 (2014). https://doi.org/10.1063/1.4890578

[12] Baril, N. F. *et al*. Growth of III-V Infrared Detector Device Layers on The AlSb Lattice Via Metamorphic Buffer Layers. in *Quantum Structure Infrared Photodetectors (QSIP) International Conference, Poland* (2022).

[13] Lubyshev, D. *et al*. Manufacturable MBE growth process for Sb-based photodetector materials on large diameter substrates. *Proc. SPIE* **8268**, 82681A (2012). https://doi.org/10.1117/12.909571

[14] Lubyshev, D. *et al*. MBE growth of Sb-based type-II strained layer superlattice structures on multi wafer production reactor. *Proc. SPIE* **7660**, 76601J (2010). https://doi.org/10.1117/12.851053

[15] Ting, D. Z. *et al*. Advances in III-V semiconductor infrared absorbers and detectors. *Infrared Phys. Technol.* **97**, 210–216 (2019). https://doi.org/10.1016/j.infrared.2018.12.034

[16] Ting, D. Z. *et al*. Long and very long wavelength InAs/InAsSb superlattice complimentary barrier infrared detectors. *J. Electron. Mater.* **51**, 4666–4674 (2022). https://doi.org/10.1007/s11664-022-09561-3

[17] Shao, H., Li, W., Moscicka, D. & Wang, W. I. Type-II InAs/GaSb superlattices grown on GaSb (311)B by molecular beam epitaxy for long-wavelength infrared applications. *J. Vac. Sci. Technol. B* **24**, 2144 (2006). https://doi.org/10.1116/1.2214705